Applied Physics Letters

Investigation of a submerging redox behavior in Fe_2O_3 solid electrolyte for resistive switching memory

Cite as: Appl. Phys. Lett. **114**, 163506 (2019); https://doi.org/10.1063/1.5089147
Submitted: 16 January 2019 . Accepted: 10 April 2019 . Published Online: 24 April 2019

Guangdong Zhou, Xiude Yang, Lihua Xiao, Bai Sun, and Ankun Zhou

Applied Physics Letters ARTICLE scitation.org/journal/apl

Investigation of a submerging redox behavior in Fe_2O_3 solid electrolyte for resistive switching memory

Cite as: Appl. Phys. Lett. **114**, 163506 (2019); doi: 10.1063/1.5089147
Submitted: 16 January 2019 · Accepted: 10 April 2019 ·
Published Online: 24 April 2019

Guangdong Zhou,[1,2,a)] Xiude Yang,[2] Lihua Xiao,[1] Bai Sun,[3,a)] and Ankun Zhou[4,5]

AFFILIATIONS

[1]School of Science, Guizhou Institute of Technology, Guiyang 550003, China
[2]School of Physical Science and Technology, Southwest University, Chongqing 400715, China
[3]School of Physical Science and Technology, Southwest Jiaotong University, Chengdu, Sichuan 610031, China
[4]Kunming Institute of Botany, Chinese Academy Science, Kunming 650201, China
[5]Department of Chemistry, Tsinghua University, Beijing 100084, China

[a)]**Electronic addresses:** zhougd@swu.edu.cn and bsun@swjtu.edu.cn

ABSTRACT

A redox reaction submerged by a high current magnitude is impressively observed in a Fe_2O_3 solid electrolyte-based resistive memory device at room temperature. Oxygen vacancy migration, Ag atom redox, phase-induced grain boundary, and water molecule interplay with the oxygen vacancy are responsible for the submerged redox behaviors. The observation of the submerged redox behavior in the Fe_2O_3 phase change process gives an insight into the evolution of memristors.

Memristors characterized by the resistive switching (RS) behavior have shown great progress and breakthrough due to the continuous material discovery, structure design, and theoretical calculations.[1–3] Because of this, the better data storage, logical memory gate, and artificial intelligence are developing.[4–6] The RS materials contain natural organics (i.e., silk proteins and egg albumen),[7,8] synthesized organics,[9] oxides (i.e., FeO_x, TiO_2, HfO_2, and TaO_x),[10–13] and doped semiconductors.[14] It has been widely accepted that Ag or Cu as an active electrode is oxidized to Ag^+ or Cu^{2+} and then is reduced to Ag or Cu atoms in the side of the counter electrode to form a metallic conduction filament, which can trigger the RS behavior in organic-based memory cells.[15,16] For organic-inorganic based devices, the migration and redistribution of active ions inside the hybrid function layer are the primary factor for the RS behaviors.[15,17]

The electrons tunneling and transferring between the Schottky potential and depletion layer are responsible for the RS behavior of the doped semiconductor.[6,18] In oxide-based devices, the variety of RS behaviors are possibly dominated by the diffusion of oxygen vacancies (V_o), migration of ions, or redox reaction.[19,20] For that, Valov has stressed that the physical model has to be extended to understand the RS behaviors.[21] Recently, Valov has stressed that the interfacial metal-oxide interactions play a dominated role in the RS behavior.[22] Tappertzhofen has reported that a redox-related initial state possibly exists in various RS behaviors before it enters into the RS regime.[23] The redox-related initial state before the RS triggered is possibly reserved during the data storage process and evolves to be a RS regime. However, the initial state is hardly detected because of a low current density.

In this letter, the submerged redox behavior is observed in the Fe_2O_3-based memory cells during the phase change process. The V_o compensation, charge release, and ion migration are systemically discussed. Based on the experiment and calculation, a physical model has been proposed for the redox-based initial stage.

10 mg of γ-Fe_2O_3 nanopowder is ultrasonically dispersed in 1 ml of N-Methyl-2-pyrrolidone solution and continuously stirred for 12 h. The precursor solution was spin-coated on the F-doped SnO_2 (FTO) substrate at 4000 rpm for 20 s to form the γ-Fe_2O_3 films. The γ-Fe_2O_3|FTO samples were dried at 85 °C for 24 h. The samples were annealed at 200, 300, 400, 500, and 600 °C in air ambient for 3 h. Ag electrodes with a diameter of 200 μm were fabricated by sputtering. Thus, the Ag| Fe_2O_3|FTO device was developed.

FeO_x has played an important role in the comprehension of the RS behaviors. This could be attributed to the rich electrochemical property of the FeO_x film: (i) valance change between Fe^{2+} and Fe^{3+};

(ii) phase change between γ and α; (iii) migration of V_o.[24–26] An obvious RS behavior is expectedly observed in the control device [Fig. 1(a)]. In the 1st stage, the high resistance state (HRS) is well kept in the sweep voltage range of 0 to 1.85 V (V_{SET}). In the 2nd stage, in the sweep voltage range (1.85 → 2.0 V), the current sharply increases from 1.83×10^{-4} A to 1.0×10^{-2} A, namely, the device switches from HRS to the low resistance state (LRS). In the 3rd and 4th stages, the LRS is well maintained in the sweep voltage range (2.0 → 0 → −2.0 → −1.25 V). In the 5th stage, the device switches from the LRS to the HRS when the bias voltage exceeds −1.25 V (V_{RESET}).

No redox peaks are observed in the control device. A weak oxidized peak located at 0.85 V (V_{ox}) is observed in the 200 °C device [Fig. 1(b)]. When the annealed temperature is increased to 300 °C, the device shows an abnormal RS behavior in the sweep voltage range (2 → 0 V): (i) the RS shows a self-limited property; (ii) the current slightly increases and then decreases, just likes an uncomplete SET process; and (iii) then, the current presents uncomplete SET behaviors. Therefore, these oxidized current peaks (J_{ox-1} and J_{ox-2}) located at 1.62 (V_{ox-1}) and 0.93 V (V_{ox-2}) are observed in the 300 °C device [Fig. 1(c)]. Similarly, two oxidized peaks located at 1.65 and 1.13 V are observed in the 300 °C device [Fig. 1(d)]. Obvious oxidized current peaks (J_{ox-1} and J_{ox-2}) and the reductive current peak (J_{red}) located at 0.93, 0.53, and −1.02 V are observed in the 500 °C device [Fig. 1(e)], respectively. However, these redox peaks become very weak for the 600 °C device [Fig. 1(f)].

The initial stage exhibits a redox-based capacitance state, in which the *I-V* curve is non-zero-crossing.[20,21] At a voltage sweep rate of 0.5 V/s, the redox current densities of $J_{p\text{-}ox.1} \sim 0.11$ A/cm^2, $J_{p\text{-}ox.2} \sim 0.29$ A/cm^2, and $J_{p\text{-}red} \sim 0.15$ A/cm^2 are observed in the 500 °C device [Fig. 2(a)]. Based these redox current values, the concentration of the diffusion of ions is estimated by the discharge current.[27] Figure 2(b) shows the time evolution vs discharge current (for V = 0) for $J_{p\text{-}ox.1}$, and the inset shows the schematic of the discharge current measurement. According to the time evolution vs the discharge current curve, the integration area denotes the number of charges (0.035 C) during the first oxidization reaction process. Similarly, the charges of the second oxidization [Fig. 2(c)] and reduced reaction [Fig. 2(d)] are 1.302 and 1.406 C, respectively. These processes are estimated by the Randles-Sevcik equation[27,28]

$$J_{p-redox} = 2.99 \times 10^5 \times Z^{\frac{3}{2}} \times C_{redox} \times \sqrt{\alpha \vartheta D_{redox}}. \quad (1)$$

Here, J_p is the redox-based peak current density (A/cm^2) and Z is the number of electrons transferred during the redox reaction process. Z is one because only one electron is transferred during the redox processes ($Ag \rightleftharpoons Ag^+ + e$, or $Fe^{2+} \rightleftharpoons Fe^{3+} + e$). C_{redox} is the ion concentration in mole per cubic centimeter, D_{redox} the ion diffusion coefficient in centimeter square per second, $\alpha \approx 0.5$ the charge transfer coefficient, and $\upsilon = 0.5$ V/s the bias voltage sweep rate. C_{redox} is calculated using Q_{redox}. It is noted that the magnitude of fixed charge of Q_f stored in the Fe_2O_3 film ($\sim 10^{-10}$ C) and the cell geometry capacitance of C_{cell} ($\sim 10^2$ pF) are insignificant compared to the Q_{redox}. Using Eq. (1), D_{redox} can be calculated by the Nernst-Einstein relation[20,28]

$$\mu = \frac{D_{redox} Ze}{K_B T}. \quad (2)$$

At room temperature (RT), using D_{redox}, the number of transferred electrons and the ion mobility μ (cm^2/Vs) can be calculated. For the first oxidization, $J_{p\text{-}ox.1}$ is 0.11 A/cm^2, $Q_{ox.1}$ is 0.035 C electrons for integration, and $C_{ox.1}$ is 0.15 mol/cm^3. Using Eq. (1), the diffusion coefficient $D_{ox.1}$ of 5.768×10^{-12} cm^2/s can be obtained. Using Eq. (2), the ion mobility $\mu_{ox.1}$ of 2.21×10^{-10} cm^2/Vs can be obtained. For the second oxidization, the $J_{p\text{-}ox.2}$, $Q_{ox.2}$, $C_{ox.2}$, $D_{ox.2}$, and $\mu_{ox.2}$ values are 0.29 A/cm^2, 1.302 C, 5.7 mol/cm^3, 2.24×10^{-16} cm^2/s, and 8.6×10^{-15} cm^2/Vs, respectively. Similarly, the $J_{p\text{-}red}$, Q_{red}, C_{red}, D_{red}, and μ_{red} values are 0.15 A/cm^2, 1.406 C, 6.15 mol/cm^3, 7.07×10^{-16} cm^2/s, and 2.71×10^{-14} cm^2/Vs for the reduced reaction

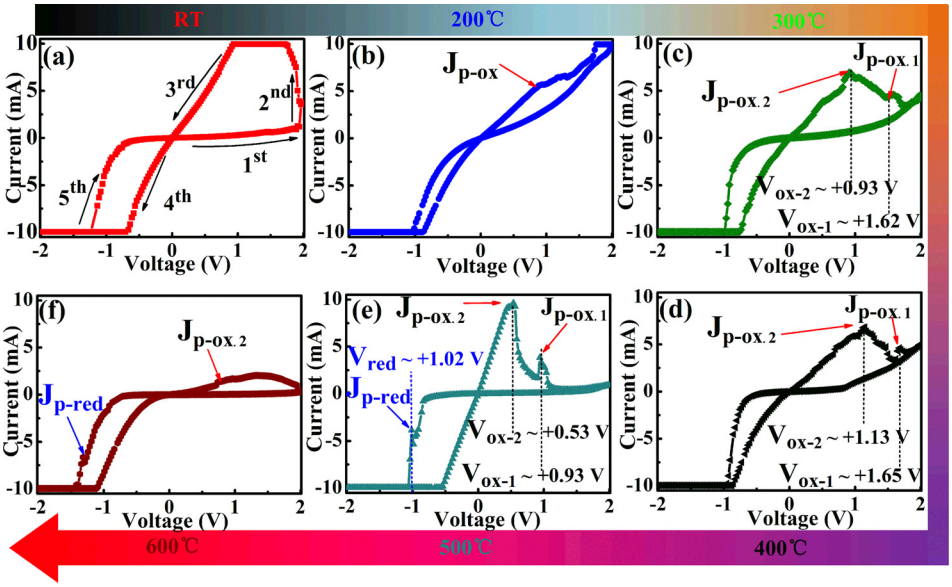

FIG. 1. I-V curves of the γ-Fe_2O_3-based device annealed at (a) room temperature, (b) 200 °C, (c) 300 °C, (d) 400 °C, (e) 500 °C, and (f) 600 °C in air ambient. Redox behaviors are observed during the phase change process. The relative humidity is 43%–60%.

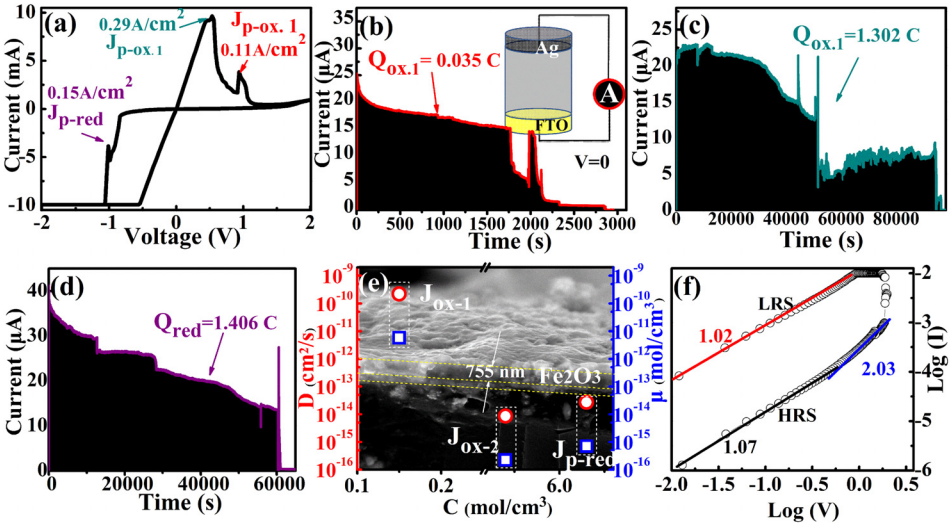

FIG. 2. (a) $J_{p\text{-}ox.1}$, $J_{p\text{-}ox.2}$, and $J_{p\text{-}red}$ of the Fe_2O_3 device annealed at 500 °C. Estimated charges of oxidized ions for (b) $J_{p\text{-}ox.1}$, (c) $J_{p\text{-}ox.2}$, and (d) $J_{p\text{-}red}$ are 0.035, 1.302, and 1.406 C, respectively, and the inset shows the schematic of the charge release measurement. (e) The ion diffusion coefficient (D_{ox} or D_{red}) and mobility (μ) vs the ion concentration (C_{ox} or C_{red}) for $J_{p\text{-}ox.1}$, $J_{p\text{-}ox.2}$, and $J_{p\text{-}red}$ are given, and the background shows a FE-SEM image of a cross-section of the Fe_2O_3|FTO sample. (f) The double-log I-V curves and fitting results for the 500 °C device.

process, respectively [Fig. 2(e)]. It is found that the ion concentration for the second oxidization is much higher than the first one. Therefore, the oxidization process is mainly dominated by the second process. Taking into account that the active Ag electrode oxidization contributed more than the Fe^{2+} oxidization process, the Ag-based redox process mainly dominates the oxidization process. The total ions of the oxidization process ($C_{ox.1} + C_{ox.2} = 5.85\ mol/cm^3$) nearly approach the reduced ion concentration ($C_{red} = 6.15\ mol/cm^3$). The gap illustrates the others (such as Sn^{4+} existing in bottom electrodes) might also contribute to the reduced process. A conclusion is made: the lower the ions concentration, the higher the diffusion coefficient and mobility. Therefore, we have deduced that the active ions (Ag^+) have a low concentration and high diffusion/mobility in the Fe_2O_3 film in the low bias region, but the case is reversed in the high bias region.

Based on the above analysis, it is found that a few Fe^{2+} ions oxidized to Fe^{3+} might dominate the first oxidization process and the Fe^{2+} ions might rapidly diffuse into the α-Fe_2O_3 matrix (2.0 V–0.93 V). After that, the ion concentration is improved by the second oxidization process, the Ag-based oxidization (0.93 V–0.53 V). In the reduced process (−1.12 V to −0.93 V), the Ag^+ ions are reduced to the Ag atom and then form a metallic conductive filament, resulting in the device that enters into the LRS state. The double-log I-V curves and the corresponding fitting results are obtained [Fig. 2(f)]. In the low electric field of the HRS, the slope is 1.07, but in a relative high electric field, the slope is 2.03. The slopes of 1.07 and 2.03 imply that the memory device of HRS is dominated by the Ohmic-like conduction in the low electric field region and Child's square law in the high electric region.[29–32] Thus, both V_o migration and Ag redox-based filaments cocontribute to the RS behaviors. For the α-Fe_2O_3-based devices, the I-V fitting illustrates that the electrons injected from electrodes are trapped by the trap sites, such as V_o and grain boundary defects.

To further verify the defects, XRD and XPS measurements are operated. Crystal planes of [211], [220], [310], [311], [222], [400], [511], and [440] originate from γ-Fe_2O_3 (JCPDS, No. 39–1346) as shown in Fig. 3(a). One can see that all the crystal planes do not show obvious changes after being annealed at 200–400 °C. Thus, the crystal phase of γ-Fe_2O_3 can be well maintained before 400 °C annealing. However, the crystal planes of [012], [104], [110], [113], [202], [024], [116], [018], and [214] characterized by α-Fe_2O_3 (JCPDS, No. 33-0664) are observed when annealing temperature exceeds 500 °C.

The binding energy peaks of Fe $2p^{3/2}$ and Fe $2p^{1/2}$ located at 710.35 eV and 724.0 eV lead to a spin-splitting energy of 13.65 eV for the control sample [Fig. 3(b)]. It demonstrates that the valance of Fe is mainly +3 for the control sample. The spin-splitting energy has a negligible shift for the 200, 300, and 400 °C samples but becomes narrow for the 500 and 600 °C samples. At the O 1s core level, two binding energy peaks located at 530.0 eV and 531.8 eV are observed for the sample annealed at 300 °C [Fig. 3(c)]. Therefore, the crystalline structure may be well maintained, but the decomposition of a nanoscale particle or generation of a new iron oxide takes place in the Fe_2O_3 film. The O 1s binding energy peaks gradually shift from 530.0 eV to 529.05 eV when the annealing temperature exceeds 500 °C. The above XPS measurements illustrate that the oxygen atom stoichiometry of the 500 or 600 °C sample is richer than others. Therefore, V_o is efficiently compensated during the annealing process.

Figure 4(a) shows the HR-TEM (JSM-2100) image of the control sample, and the lattice constants in the selected region are 2.50 Å and 2.95 Å, which originate from the lattice planes of [311] and [220],

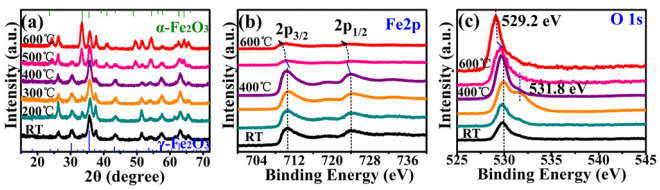

FIG. 3. (a) XRD spectra of γ-Fe_2O_3 thin films annealed at different temperatures in air ambient; XPS spectra of core levels of (b) Fe 2p and (c) O 1s for the γ-Fe_2O_3 films annealed at different temperatures.

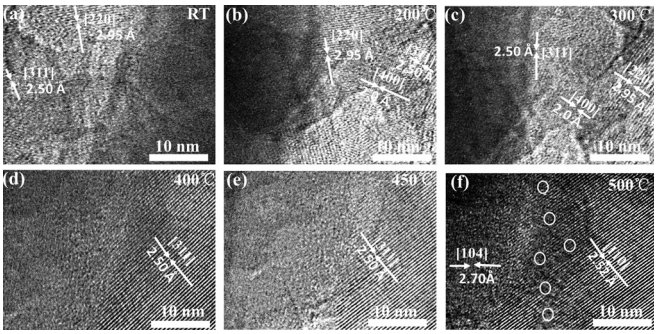

FIG. 4. HR-TEM of the γ-Fe_2O_3 samples annealed at different temperatures of (a) room temperature (RT), (b) 200 °C, (c) 300 °C, (d) 400 °C, (e) 450 °C, and (f) 500 °C.

respectively. The lattice constants of 2.50 Å and 2.95 Å are well maintained, and a lattice plane of [400] with a lattice constant of 2.0 Å is observed for the Fe_2O_3 sample annealed at 200 °C [Fig. 4(b)]. [311] shows no change for the 300–450 °C samples [Figs. 4(c)–4(e)]. [110] and [104] of α-Fe_2O_3 are detected for the 500 °C sample [Fig. 4(f)]. The lattice defects labeled by the white cycle in Fig. 4(f) are observed for the 500 °C sample. Therefore, tremendous grain boundary defects are generated during the phase change.

V_o is inevitably generated during film fabrication process, but V_o is partially compensated during the annealing process.[33] Therefore, the V_o concentration of α-Fe_2O_3 is lower than that of γ-Fe_2O_3. The redox reaction process is not observed in the control device [Fig. 1(a)] but can be observed in Ag|α-Fe_2O_3|FTO [Fig. 1(e)]. Ions and electrons migrated along grain boundary defects have contributed to the redox process.[34,35] Therefore, boundary defects-based reactions are responsible for the enhanced redox behavior. In Ag|γ-Fe_2O_3|FTO, the grain boundary defects are negligible because of a low concentration, while the high concentrations of V_o and Ag^+ are the main factors. In the Ag|α-Fe_2O_3|FTO, the V_o-based conductive path weakens due to the compensation effect,[34,36] while the interplay between water molecule

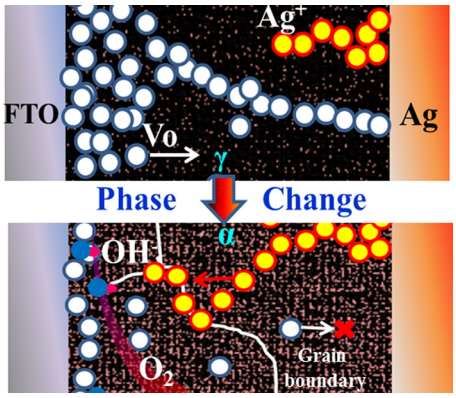

FIG. 5. The migration of V_o, phase change-induced water splitting, and migration of Ag^+ for the Fe_2O_3-based RS device.

and interface V_o is enhanced for the rich-defect sample (Fig. 5). Therefore, three redox reactions are possible: (i) water splitting ($O_2 + 2H_2O + 4e^- \rightleftharpoons 4OH^-$; $H_2O + O_O^{\times} + V_o \rightleftharpoons 2OH^-$),[19,34,37] (ii) Ag ionization ($Ag \rightleftharpoons Ag^+ + e^-$),[8,35] and (iii) Electron hop ($Fe^{3+} + e^- \rightleftharpoons Fe^{2+}$).[29] In these reactions, water and Ag ionization are the dominating factors and the electron hop effect is considered second.

In summary, a redox reaction submerged by a high current magnitude in a Fe_2O_3 solid electrolyte-based memory device is impressively observed during the Fe_2O_3 phase change process. The V_o migration, iron ion redox, Ag atom redox, and water splitting facilitated by the grain boundary generated during the phase change are responsible for the RS behaviors.

We thank the Support Plan for Postdoctoral Innovative Talents of Chongqing (CQBX201806) for funding support.

REFERENCES

[1]S. Kumar, J. P. Strachan, and R. S. Williams, Nature **548**, 318 (2017).
[2]T. Kawashima, K. S. Yew, Y. Zhou, D. S. Ang, H. Z. Zhang, and K. Kyuno, Appl. Phys. Lett. **112**, 213505 (2018).
[3]M. S. Kadhim, F. Yang, B. Sun, Y. Wang, T. Guo, Y. Jia, and Y. Zhao, Appl. Phys. Lett. **113**, 053502 (2018).
[4]M. A. Zidan, J. P. Strachan, and W. D. Lu, Nat. Electron. **1**, 22–29 (2018).
[5]Z. Wang, S. Kumar, H.-S. P. Wong, and Y. Nishi, Appl. Phys. Lett. **112**, 073102 (2018).
[6]G. D. Zhou, B. Sun, Y. Yao, H. Zhang, A. Zhou, K. Alameh, B. Ding, and Q. Song, Appl. Phys. Lett. **109**, 143904 (2016).
[7]H. Wang, B. Zhu, X. Ma, Y. Hao, and X. Chen, Small **12**, 2715–2719 (2016).
[8]G. D. Zhou, Y. Q. Yao, Z. S. Lu, X. D. Yang, J. J. Han, G. Wang, Q. Liu, and Q. L. Song, Nanotechnology **28**, 425202 (2017).
[9]B. Sun, X. Zhang, G. D. Zhou, P. Li, Y. Zhang, Y. Xia, and Y. Zhao, Org. Electron. **42**, 181–186 (2017).
[10]T. Ishibe, T. Kurokawa, N. Naruse, and Y. Nakamura, Appl. Phys. Lett. **113**, 141601 (2018).
[11]H. Ni, M. Zheng, L. Chen, W. Huang, Y. Qi, J. Zeng, and J. Gao, Appl. Phys. Lett. **110**, 213503 (2017).
[12]Y. Chen, S. Zhu, Q. Wei, Y. Xia, A. Li, and J. Yin, Appl. Phys. Lett. **112**, 063503 (2018).
[13]B. Wang, K. H. Xue, H. J. Sun, Z. N. Li, N. Liu, B. Y. Tian, X. X. Liu, and X. S. Miao, Appl. Phys. Lett. **113**, 183501 (2018).
[14]W. R. Acevedo, C. Acha, M. J. Sánchez, P. Levy, and D. Rubi, Appl. Phys. Lett. **110**, 053501 (2017).
[15]Y. Wang, Z. Lv, Q. Liao, H. Shan, J. Chen, Y. Zhou, L. Zhou, X. Chen, V. A. L. Roy, Z. Wang, Z. Xu, Y.-J. Zeng, and S.-T. Han, Adv. Mater. **30**, 1800327 (2018).
[16]B. Sun, L. Wei, H. Li, X. Jia, J. Wu, and P. Chen, J. Mater. Chem. C **3**, 12149–12155 (2015).
[17]C. Gu and J.-S. Lee, ACS Nano **10**, 5413–5418 (2016).
[18]M. Ungureanu, R. Zazpe, F. Golmar, P. Stoliar, R. Llopis, F. Casanova, and L. E. Hueso, Adv. Mater. **24**, 2496–2500 (2012).
[19]I. Valov and W. D. Lu, Nanoscale **8**, 13828–13837 (2016).
[20]I. Valov and T. Tsuruoka, J. Phys. D: Appl. Phys. **51**, 413001 (2018).
[21]I. Valov, E. Linn, S. Tappertzhofen, S. Schmelzer, and R. Waser, Nat. Commun. **4**, 1771 (2013).
[22]D. Cho, M. Lübben, S. Wiefels, K. Lee, and I. Valov, ACS Appl. Mater. Interfaces **9**, 19287–19295 (2017).
[23]S. Tappertzhofen, I. Valov, T. Tsuruoka, T. Hasegawa, R. Waser, and M. Aono, ACS Nano **7**, 6396–6402 (2013).
[24]J. Y. Lee, Y. J. Baek, Q. Hu, and Y. J. Choi, Appl. Phys. Lett. **102**, 122111 (2013).

[25]J. Jeon, J. Jung, and K. H. Chow, Appl. Phys. Lett. **111**, 242401 (2017).
[26]X. Huang, K. Jiang, Y. Niu, R. Wang, D. Zheng, A. Dong, X. Dong, C. Mei, J. Lu, S. Liu, Z. Gan, N. Zhong, and H. Wang, Appl. Phys. Lett. **113**, 112103 (2018).
[27]S. Tappertzhofen, S. Menzel, I. Valov, and R. Waser, Appl. Phys. Lett. **99**, 203103 (2011).
[28]A. Bard and L. Faulkner, *Electrochemical Methods: Fundamentals and Applications* (Wiley, New York, 2001).
[29]G. D. Zhou, B. Wu, X. Liu, Z. Li, S. Zhang, A. Zhou, and X. Yang, J. Alloys Compd. **678**, 31–35 (2016).
[30]L. Hu, S. Zhu, Q. Wei, Y. Chen, J. Yin, Y. Xia, and Z. Liu, Appl. Phys. Lett. **113**, 043503 (2018).
[31]G. D. Zhou, L. H. Xiao, S. J. Zhang, B. Wu, X. Liu, and A. K. Zhou, J. Alloys Compd. **722**, 753–759 (2017).
[32]Y. Tao, X. Li, Z. Wang, H. Xu, W. Ding, J. Ma, and Y. Liu, Appl. Phys. Lett. **111**, 183504 (2017).
[33]B. Mace, Z. Harrell, C. Chen, E. Enriquez, A. Chen, and Q. Jia, Appl. Phys. Lett. **112**, 073905 (2018).
[34]G. D. Zhou, S. K. Duan, Y. Yao, B. Sun, Y. Yao, X. Yang, J. Han, J. Wu, C. Y. Xu, D. Liu, T. Chen, L. Chen, A. K. Zhou, and Q. L. Song, Adv. Electron. Mater. **4**, 1700567 (2018).
[35]G. D. Zhou, Z. S. Lu, Y. Q. Yao, G. Wang, A. K. Zhou, P. Li, B. F. Ding, and Q. L. Song, J. Appl. Phys. **121**, 155302 (2017).
[36]C. Hu, Q. Wang, S. Bai, M. Xu, D. He, and D. Lyu, Appl. Phys. Lett. **110**, 073501 (2017).
[37]S. Tappertzhofen, H. Mundelein, I. Valov, and R. Waser, Nanoscale **4**, 3040–3043 (2012).